

A Piezoelectric-Driven Three-Dimensional MEMS VOA Using Attenuation Mechanism With Combination of Rotational and Translational Effects

Kah How Koh, Chengkuo Lee, *Member, IEEE*, and Takeshi Kobayashi

Abstract—A gold-coated silicon mirror (5 mm × 5 mm) actuated by piezoelectric Pb(Zr, Ti)O₃ (PZT) cantilever beams has been investigated for variable optical attenuator applications. The device is micromachined from a SOI substrate with a 5- μ m-thick Si device layer, with multilayers of Pt/Ti/PZT/Pt/Ti deposited as electrode materials. A large Si mirror plate and 1 × 10 arrayed PZT cantilevers arranged in parallel are formed after the release process. The ten cantilevers are designed to be electrically isolated from one another. A dual-core fiber collimator is aligned perpendicularly to the mirror in a 3-D light attenuation arrangement. Thus, three modes of attenuation mechanisms were investigated based on rotational and translational effects. A dynamic attenuation range of 40 dB is achieved at 1 V and 1.8 V for bending and torsional mode, respectively. [2010-0097]

Index Terms—Microelectromechanical systems (MEMS), mirror, optical microelectromechanical systems, piezoelectric actuator, PZT, variable optical attenuator.

I. INTRODUCTION

OPTICAL microelectromechanical systems (MEMS) technology has been an enabling tool for numerous cutting-edge devices for applications such as displays [1], optical coherence tomography [2], and optical communication [3]. Cornerstones for the success of optical MEMS technology include actuator technology, optics design, and development of movable or tunable micromechanical elements, e.g., rigid reflective mirrors [4], deformable reflective mirrors [5], shutters [6], gratings [7], [8], waveguides [9], and sliding blades [10]. Combining the surface micromachined polycrystalline silicon (polySi) mirrors with electrostatic or thermal actuation mechanism has been the mainstream optical MEMS technology in the late 90s [11]–[13]. However, the flat polySi mirror is typically achieved only within mirror size of a few hundreds of micrometers due to the mirror bending issue caused by residual

stress. Thus, single crystalline silicon mirrors of 1 mm² ~ a few millimeter square has been developed to fulfill such technology gap, i.e., demands of large flat mirrors [4], [14]. Deep reactive ion etching (DRIE) of silicon-on-insulator (SOI) substrate and CMOS micromachining are major approaches for enabling large and flat silicon mirrors, while the actuation mechanisms include electrostatic [4], [14]–[20], magnetic [21]–[24], thermal [25]–[27], and piezoelectric [28]–[30]. Design of optics and their integration with large mirrors is typically realized in 3-D configurations, while the pop-up polySi mirrors can easily align and integrate with binary optics, optical fibers, and waveguides on top of substrates in 2-D-like approaches, i.e., planar configurations [31], [32].

To achieve large mechanical rotation angles, gimballed mirrors using torsion springs are the popular design for integration with various actuators such as electrostatic, magnetic, and piezoelectric [4], [17], [19]–[21], [29]–[31]. On the other hand, thermal bimorph actuator provides large mechanical deflection angle to mirrors with large mechanical deflection angles [25]–[27]. The display can be realized by on/off switched micromirror arrays [33], grating arrays [34], and a single raster scanning mirror at its resonant mode operation [17], [22]. In contrast, applications in optical communication normally require both static and dynamic operations of the mirrors, shutters, or gratings. It implies that in addition to good dynamic characteristics, large static displacement, large static deflection angle, or large static rotation angle are expected for these optical MEMS devices for communications. Optical MEMS devices in optical communication applications are known as tunable lasers [3], [13], [35], [36], optical switches [13], [32], [37], reconfigurable add/drop multiplexers [13], [38], [39], and variable optical attenuators (VOAs) [13], [40]. Due to their widespread presence in optical networks, a large number of VOAs are currently used in wavelength multiplexing and demultiplexing nodes of dense wavelength division multiplexer systems to control the transmission power of optical signals.

By using a polySi micromirror arranged between the coaxially aligned input and output fibers [41], this micromirror functions as a shutter and can move in an out-of-plane direction with a given bias due to electrostatic force. The attenuation of this MEMS VOA is determined as a function of the position of the micromirror, i.e., the percentage of blocked light. The DRIE-made silicon shutter has been known as another shutter type of MEMS VOAs [42]. In addition to the shutter type MEMS VOAs [41]–[44], there are two more groups of

Manuscript received April 8, 2010; revised August 18, 2010; accepted August 19, 2010. Date of publication October 7, 2010; date of current version November 30, 2010. This work was supported by the National University of Singapore under Grant R-263-000-475-112. The work of K. H. Koh was supported by a Ph.D. scholarship grant from GLOBALFOUNDRIES, Singapore. Subject Editor S. Merlo.

K. H. Koh and C. Lee are with the Department of Electrical and Computer Engineering, National University of Singapore, Singapore 117576 (e-mail: g0900280@nus.edu.sg; elelc@nus.edu.sg).

T. Kobayashi is with the National Institute of Advanced Industrial Science and Technology (AIST), Tsukuba 305-8564, Japan (e-mail: takeshi-kobayashi@aist.go.jp).

Color versions of one or more of the figures in this paper are available online at <http://ieeexplore.ieee.org>.

Digital Object Identifier 10.1109/JMEMS.2010.2076785

MEMS VOAs. They are the planar reflective type [45]–[54] and the 3-D reflective-type [55]–[58]. In the planar reflective type MEMS VOA, attenuation is achieved due to the change in coupling efficiency between the input and output fiber when the mirror is actuated. For example, H. Cai *et al.* have implemented an electrostatic actuated elliptical mirror with the input and output fibers positioned at the two focal centers of the reflective elliptical mirror [49]. This VOA design has low polarization dependence loss (PDL) and low wavelength dependent loss (WDL), and it achieves 44 dB attenuation with a 10.7 V dc.

General speaking, an attenuation scheme based on the microshutter design offers the benefits of low insertion loss (IL) and large attenuation range due to the close proximity between the input and output optical fibers. However, it also results in a large PDL and a strong back reflection due to the diffraction and the coaxial assembly, respectively. On the other hand, the planar reflective mirror type of attenuation mechanism offers low PDL and low WDL, but suffers from high IL due to a certain amount of separation needed for fiber assembly.

Combining optics and a reflective mirror to be assembled in a 3-D configuration is also a key approach in making MEMS VOA devices. In conjunction with large microoptics such as dual-core collimators, such a 3-D VOA device can gain excellent data of return loss, PDL, and WDL under reasonable driving voltage. K. Isamoto *et al.* reported an electrostatic torsional mirror operated at 4.5 V for 40 dB attenuation with a dynamic response time of 5 ms [55]. Besides using a large single reflective mirror, an array of small mirrors is used to replace the single reflective mirror and form a multibit digital VOA [56], [57]. While Riza and Ghauri deployed commercial digital micromirror device for enabling digital VOA. W. Sun *et al.* reported a digital VOA comprising an array of 16 equal-length rectangular micromirrors. The linear attenuation was achieved by switching individual mirrors of the array. Piezoelectric-actuated 3-D MEMS VOA has been reported for 40 dB attenuation at 1 V dc by using two PZT thin-film actuators on two sides of a torsional mirror [58].

Moreover, new progress in the actuation mechanism for VOA has also been reported in recent literature. Variable optical attenuators based on optofluidic technology have also been demonstrated in recent years. For example, H. Yu *et al.* have developed a transmission-type VOA with an air-controlled membrane made of polydimethylsiloxane (PDMS) [59]. When the membrane deforms, it changes the liquid dimension in the optical transmission path, hence attaining attenuation by altering the optical absorbing capability of the liquid. In another PDMS VOA fabricated by M. I. Lapsley *et al.*, attenuation is achieved by varying the refractive index of the fluid within the microchannel; hence, the reflectivity of the fluid and PDMS interface [60]. However, low voltage-driven MEMS VOAs have only been demonstrated by piezoelectric and electromagnetic actuation mechanisms [6], [58]. Limited research effort has been reported in 3-D MEMS VOAs in contrast to the reported activities in planar MEMS VOAs. Thus, we explore a new 3-D MEMS VOA driven by a piezoelectric beam actuator integrated with 1×10 PZT cantilever array. The electrical connections to each of the cantilevers are separated, hence allowing for

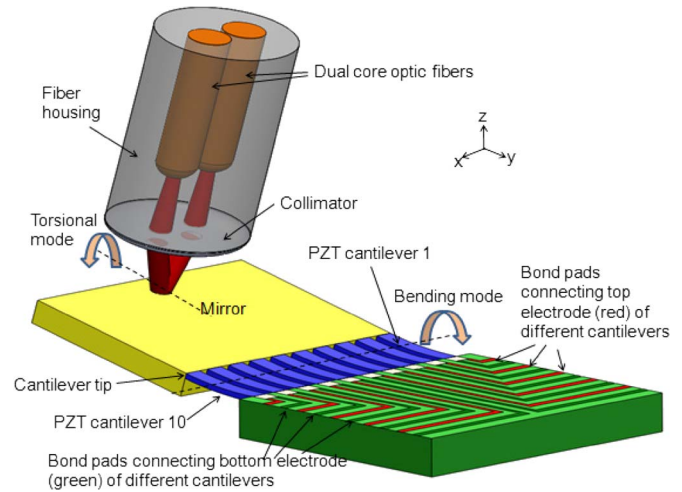


Fig. 1. Schematic drawing of PZT MEMS VOA with dual-core collimator arranged in 3-D configuration such that the light beam focuses on the far edge center of the mirror plate. Bending mode occurs when all the ten cantilevers are biased simultaneously at the same voltage. Torsional mode occurs where a set of five cantilevers bends in one direction while the other set of five cantilevers bends in the opposite direction.

TABLE I
DIMENSIONS OF 3-D MEMS VOA DEVICE

Mirror	PZT cantilevers	Si beam	Si mirror plate
5mm x 5mm	3mm long x 0.24mm wide x 3 μ m thick	3mm long x 5mm wide x 5 μ m thick	5mm long x 5mm wide x 0.4mm thick

individual biasing conditions. By addressing different bias voltages to individual PZT cantilever actuators, we achieved the translational mode (deflection mode) and rotational mode simultaneously. The attenuation efficiency of these two modes is investigated, while mixed mode is reported as well.

II. DESIGN AND MODELING

A schematic diagram of the PZT 3-D MEMS VOA demonstrated in this paper is shown in Fig. 1. The dimensions of the device are summarized in Table I. Ten patterned PZT thin-film cantilevers are arranged in parallel along one of the sides of the Si mirror; in other words, the longitudinal direction of cantilevers. The electrical connections to each cantilever are separated from one another, with individual bonding pads connected to each of the top and bottom electrodes of the cantilevers. The novelty of our design lies in the capability of mirror movement with six degrees of freedom to enable the 3-D attenuation scheme. Bending mode is elicited when all the cantilevers are biased simultaneously at the same dc voltage. As a result of the displacement introduced by the bent cantilevers under bias, the mirror undergoes translational and rotational movement along the x -axis (Fig. 2). Torsional mode is induced when, for example, cantilevers 1–5 are biased in such a way that they bend up, while cantilevers 6–10 are biased in an opposite way and bent in the opposite direction, i.e., bending downward. The difference in bending directions for the two sets of actuators causes the mirror to rotate along the y -axis (Fig. 3).

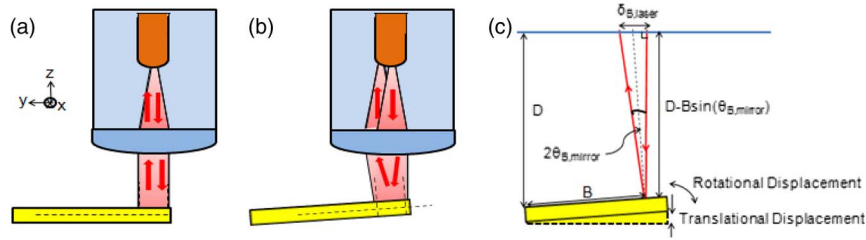


Fig. 2. Schematic diagrams showing the attenuation mechanism for bending mode: (a) configuration refers to the initial state of minimum insertion loss. All of the light beams from the input fiber are coupled back into the output fiber when the cantilevers are not biased, i.e., the mirror surface remains normal to light beam; (b) a portion of the light beam from input fiber is deviated from the optimized reflection light path when the cantilevers are biased, i.e., the mirror undergoes rotational and translational motion; (c) mirror is rotated by an angle $\theta_{B,mirror}$ and the laser beam is displaced by a distance $\delta_{B,laser}$.

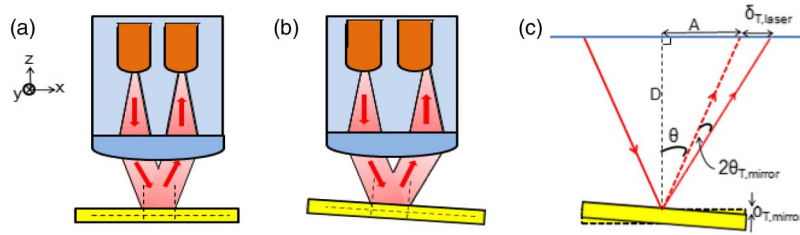


Fig. 3. Schematic diagrams showing the attenuation mechanism for torsional mode: (a) All of the light beam from the input fiber are coupled back into the output fiber when the cantilevers are not biased. It is the initial state of minimum insertion loss; (b) configuration refers to the attenuation state when a portion of the light beam from the input fiber is not coupled back to the output fiber because cantilevers 1–5 and cantilevers 6–10 are oppositely biased, i.e., the mirror undergoes rotational motion; (c) mirror is rotated by an angle $\theta_{T,mirror}$ and the laser beam is displaced by a distance $\delta_{T,laser}$.

To understand the attenuation mechanism better, schematic diagrams in Figs. 2 and 3 are used to show the two modes of attenuation operation, i.e., bending and torsional mode.

Fig. 2 shows the side profile of the mirror and the dual-core collimator under bending mode. In Fig. 2(a), when the cantilevers are not biased, the normal of the mirror surface is perfectly aligned with the light beam, coupling all the light from the input fiber to the output fiber. When the mirror translates and rotates due to a dc driving voltage simultaneously applied to the ten cantilevers as shown in Fig. 2(b), a portion of the light beam no longer couples into the output fiber, resulting in attenuation. In Fig. 2(c), both rotational and translational displacements are observed when the actuators are biased. In addition, Fig. 2(c) also allows us to build an analytical model, relating the displacement of the ten cantilevers to the displacement of the laser beam from its original position. The rotation angle of the mirror plate $\theta_{B,mirror}$ is related to the displacement of the laser beam from its original position $\delta_{B,mirror}$ by

$$\theta_{B,mirror} = \frac{2\delta_{cantilever}}{L_{cantilever}} \quad (1)$$

$$B = L_{mirror} - \cos(\theta_{B,mirror}) * R_{dot \ size} \quad (2)$$

$$\delta_{B,laser} = [D - B \sin(\theta_{B,mirror})] * \tan(2\theta_{B,mirror}) \quad (3)$$

where $L_{cantilever}$ is the length of the cantilever (3 mm), $\delta_{cantilever}$ is the displacement of the cantilever tip, L_{mirror} is the length of the mirror plate (5 mm), $R_{dot \ size}$ is the radius of the circular laser beam spot (350 μm), and D is the working distance of the dual-core collimator (1 mm). With the aforementioned (1)–(3), we are able to calculate the theoretical displacement of the laser beam from its original position

using the experimental data collected for the displacement of the dc-biased cantilever tip measured under the optical microscope.

Similar analysis was done to investigate the attenuation mechanism under torsional mode. Fig. 3 shows the front profile of the mirror and the dual-core fibers with collimator. In Fig. 3(a), perfect coupling occurs when the cantilevers are initially unbiased. In Fig. 3(b), cantilevers 1–5 and 6–10 are oppositely biased, hence introducing opposite displacements for the two sets of cantilevers. As a result, the mirror undergoes torsional rotation, reflecting a portion of the light beam away from its original position. Fig. 3(c) shows a simplified diagram of the laser beams reflected by a rotated mirror. The torsional rotation angle of the mirror $\theta_{T,mirror}$ is related to the displacement of the laser beam from its original position by

$$\theta_{T,mirror} = \tan^{-1} \left(\frac{2\delta_{T,mirror}}{L_{mirror}} \right) \quad (4)$$

$$\theta = \tan^{-1} \left(\frac{A}{D} \right) \quad (5)$$

$$\delta_{T,laser} = D * \tan(\theta + 2\theta_T) - A \quad (6)$$

where $\delta_{T,mirror}$ is the displacement of the mirror edges observed under optical microscope, L_{mirror} is the length of the mirror plate (5 mm), A is the half-distance between the input and output fiber (100 μm), and WD is the working distance of the dual-core collimator (1 mm). These (4)–(6) allow us to derive the displacement of the laser beam from its original position using the experimental $\delta_{T,mirror}$ under torsional mode.

To evaluate the quality of the fabricated piezoelectric cantilevers, a model is necessary to compute the piezoelectric

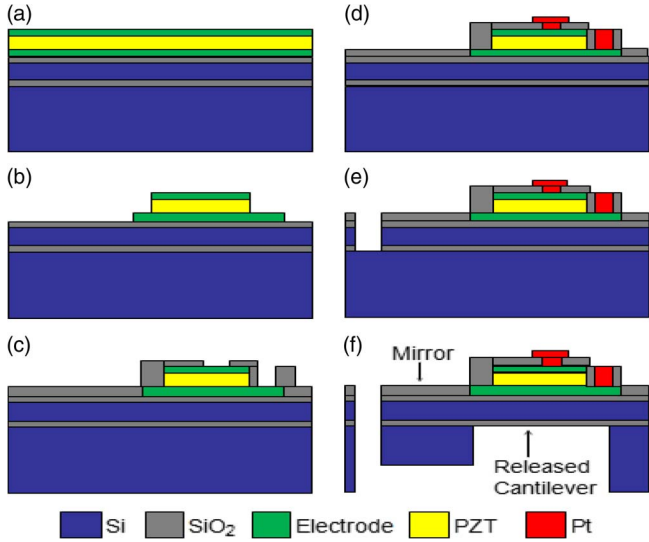


Fig. 4. Microfabrication process flow for making PZT cantilever actuators and mirror.

constant d_{31} of the PZT thin film. The following are used to find value of d_{31} [61]:

$$\delta_{\text{cantilever}} = \frac{3AB}{K} L^2 V d_{31} \quad (7)$$

$$A = S_{\text{Si}} S_{\text{PZT}} (S_{\text{PZT}} t_{\text{Si}} + S_{\text{Si}} t_{\text{PZT}}) \quad (8)$$

$$B = \frac{t_{\text{Si}} (t_{\text{Si}} + t_{\text{PZT}})}{s_{\text{PZT}} t_{\text{Si}} + s_{\text{Si}} t_{\text{PZT}}} \quad (9)$$

$$K = (S_{\text{Si}})^2 (t_{\text{PZT}})^4 + 4S_{\text{Si}} S_{\text{PZT}} t_{\text{Si}} (t_{\text{PZT}})^3 + 6S_{\text{Si}} S_{\text{PZT}} (t_{\text{Si}})^2 (t_{\text{PZT}})^2 + 4S_{\text{Si}} S_{\text{PZT}} (t_{\text{Si}})^3 (t_{\text{PZT}}) + (S_{\text{PZT}})^2 (t_{\text{Si}})^4 \quad (10)$$

where $\delta_{\text{cantilever}}$ is the displacement of the cantilever tip observed under an optical microscope, L is the length of the cantilever (3 mm); V is the applied voltage; S_{Si} and S_{PZT} are the compliances of the structural Si layer ($6.0 \times 10^{-12} \text{ Pa}^{-1}$) and PZT thin film ($1.43 \times 10^{-11} \text{ Pa}^{-1}$), respectively; and t_{Si} and t_{PZT} are the respective thicknesses of the structural silicon ($5 \mu\text{m}$) and PZT film ($3 \mu\text{m}$). From (7), it can be interpreted that the value of d_{31} can be derived from the gradient of a $\delta_{\text{cantilever}} - V$ plot.

III. DEVICE MICROFABRICATION

Fig. 4 shows the microfabrication process flow of the MEMS VOA investigated in this paper. A SOI substrate with $5 \mu\text{m}$ thick Si device layer and $1 \mu\text{m}$ thick buried oxide (BOX) layer were used as the starting material as shown in Fig. 4(a). A thermal oxide layer of $0.37 \mu\text{m}$ was first created from the Si device layer before the multilayer electrode of LaNiO_3 ($0.2 \mu\text{m}$)/ Pt ($0.2 \mu\text{m}$)/ Ti ($0.05 \mu\text{m}$) were deposited by RF (for LaNiO_3) and dc magnetron sputtering (for Pt/Ti). A $3.1 \mu\text{m}$, the PZT thin film was then deposited using sol-gel technique, which is similar to our previous efforts [62], [63]. The LaNiO_3 buffer layer, which the PZT thin film was prepared on, allows for a (100)-orientated columnar structure to be formed in

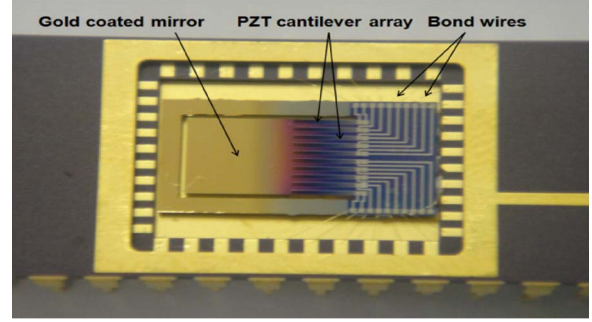


Fig. 5. Close-up photo showing the packaged PZT MEMS VOA with a gold-coated mirror surface. The bond pads are connected to the pins of the package via gold bond wires.

the PZT film [64]. This (100) crystallographic orientation helps maximize the dielectric constant and electrical properties of the PZT film [65]. The deposited films were then pyrolyzed at $200 \text{ }^\circ\text{C}$ – $470 \text{ }^\circ\text{C}$ for five minutes and crystallized by rapid thermal annealing at $700 \text{ }^\circ\text{C}$ for two minutes. Pt bottom electrode is used for its high stability in the processing temperature range. Finally, Pt/LaNiO_3 layers were sputtered on top of the PZT film to form the top electrode.

In Fig. 4(b), the top Pt thin film was etched by Ar ion while the LaNiO_3 film was subsequently etched by dilute HCl solution. The underlying PZT thin film was etched by a mixture solution of HF, HNO_3 , and HCl. The bottom LaNiO_3 / Pt/Ti electrode layers were then etched again by the same respective etchants. In Fig. 4(c), a $0.8 \mu\text{m}$ thick insulating oxide layer was deposited by RF-magnetron sputtering. Contact holes were formed by reactive ion etching (RIE) with CHF_3 gas. In Fig. 4(d), $1 \mu\text{m}$ thick Pt metal lines with Ti adhesion layer were deposited by RF-magnetron sputtering and later etched by Ar ion. In Fig. 4(e), the thermal oxide, structural Si and BOX layer were etched by RIE using CHF_3 (SiO_2) and SF_6 (Si) to define the pattern of the cantilevers and mirror. Finally, in Fig. 4(f), the Si substrate and BOX were etched from the backside using DRIE in order to release the cantilevers and mirror. The etchant gases used for Si and SiO_2 in this case are SF_6 and CHF_3 , respectively. A thick Si substrate is left beneath the mirror to maintain the rigidity and flatness of the mirror. A thin film of gold was sputtered on the mirror surface using a shadow mask. This is to ensure that the 1550 nm light gets reflected by the gold-coated mirror.

After the fabrication process, the device is bonded onto a dual inline package (DIP) and the bond pads were connected by gold bond wires to the metal pins of the DIP, as shown in Fig. 5. Fig. 6 shows the optical microscope photos taken on the various structures of the device. Fig. 6(a) shows the top and bottom electrodes for each of the PZT cantilevers while Fig. 6(b) shows the individual bond pad physically connected to an electrode, i.e., the ten cantilevers are electrically isolated from one another. In Fig. 6(c) and (d), photos on the gold-coated mirror and the parallel arranged PZT cantilevers are shown, respectively.

To enhance the piezoelectric characteristics, poling treatment was conducted on the PZT thin-film actuators at 30 V for 10 minutes at room temperature. In order to derive the value of

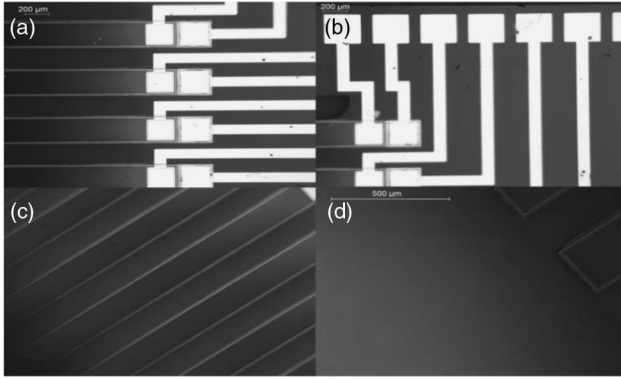


Fig. 6. Optical microscope photos of the (a) top and bottom electrodes of each cantilever; (b) bond pad each individually connected to an electrode of a cantilever; (c) PZT cantilevers arranged in parallel; and (d) gold-coated mirror surface.

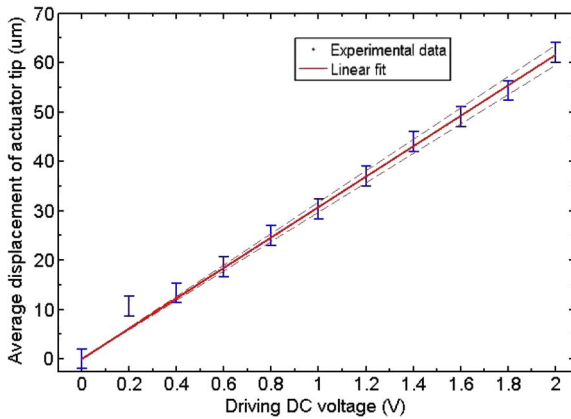


Fig. 7. Measured average displacement of cantilever tips versus dc driving voltage applied to the top electrodes of all ten cantilevers.

transverse piezoelectric constant, d_{31} , the ten cantilevers were biased simultaneously at the same dc driving voltage while the displacement of the ten cantilever tips were observed under the optical microscope. The measured displacements of ten cantilevers were averaged. This was repeated for various dc driving voltages and the results were plotted and shown in Fig. 7. A linear fit for the experimental data was also plotted, and as discussed in the previous section, the value of d_{31} can be derived from the gradient of the linear fit plotted. The transverse piezoelectric constant d_{31} is estimated as $136 \pm 4 \text{ pmV}^{-1}$.

IV. EXPERIMENTAL SETUP

The schematic drawing of the measurement setup for MEMS VOA characterization is shown in Fig. 8. A dual-core fiber with a collimator was placed at a position about 1 mm (working distance) away from the mirror surface, while the device was mounted on a multiaxis x-y-z movable stage. The input light from the 1550 nm light source was launched via one core of the dual-core fiber through the collimator to the edge of the mirror furthest away from the cantilever array, where the translational and rotational motion induced by the biased cantilevers were the biggest. This will allow for maximum attenuation at the lowest possible dc driving voltage. The reflected light was

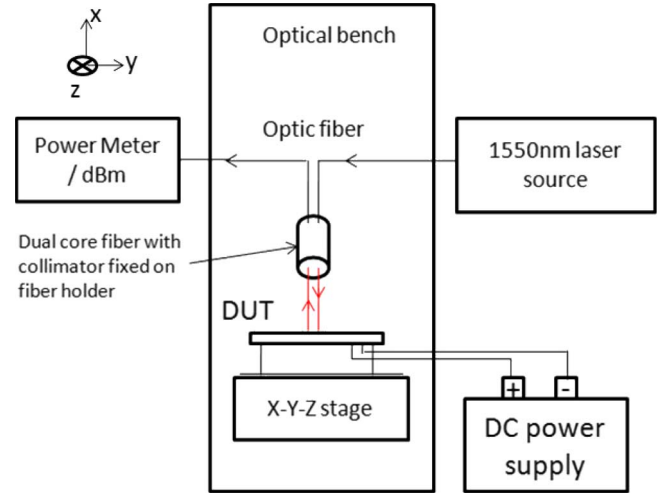


Fig. 8. Schematic drawing of the measurement setup for 3-D MEMS VOA characterization carried out on an anti-vibration optical bench. The stage is capable of moving in X-Y-Z directions and tilting along X-Y(θ_z) and Y-Z(θ_x) planes as well.

collected by the same collimator to the power meter via the output core of the dual-core fiber. The power of the 1550 nm laser source used in the experiment is 2 mW. The collimated beam diameter had been characterized to be $700 \mu\text{m} \pm 25 \mu\text{m}$. The whole setup was established on an anti-vibration optical table to prevent ambient vibration.

For the initial insertion loss measurement, the relative positions of the collimator and mirror were adjusted such that coupling loss is optimized or minimized. In order to do so, laser light of 632.8 nm was first used as the laser source. The red laser beam was shone through the collimator onto the far edge of the mirror plate. Subsequently, the x-y-z stage is adjusted to centralize the red laser spot at the far edge of the mirror. The 1550 nm laser source was then fed into the input fiber after the coarse alignment step had been confirmed. In the step of fine alignment, the position of the mirror relative to the collimator are adjusted by moving and tilting the $x-y-z-\theta_y-\theta_z$ stages such that minimum insertion loss is reached, i.e., initial insertion loss. The θ_y and θ_z adjustment knobs enable the tilting of the stage with respect to the y - and z -axis, respectively. The measured initial insertion loss in this setup is typically about $2 \sim 3 \text{ dB}$. This value is about $1 \sim 2 \text{ dB}$ higher than commercially available VOA products. It is mainly attributable to the surface roughness and warpage of the mirror. Further optimization of the mirror fabrication and microstructures may reduce the initial insertion loss to be less than 1 dB.

V. RESULTS AND DISCUSSION

A. Bending Mode

In the operation of the PZT MEMS VOA, various dc driving voltages are applied to the ten cantilevers to actuate the mirror during the process. As a result, the reflected light deviates from the optimized light path corresponding to minimum insertion loss. The coupled reflected light intensity toward the output fiber is reduced, resulting in increased insertion loss with increasing driving voltage. Based on the VOA measurement setup

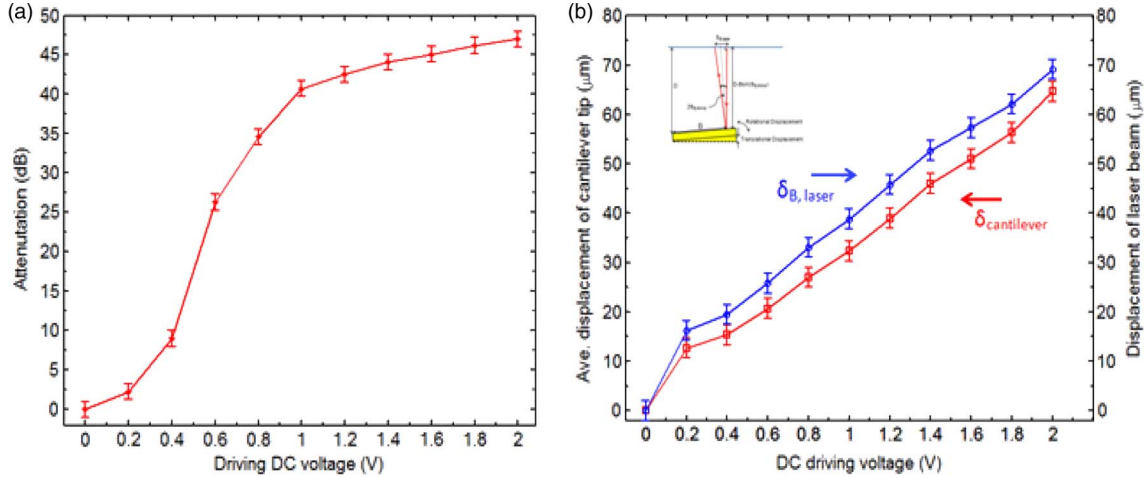


Fig. 9. Experimental data for bending mode. (a) Measured attenuation curve versus dc driving voltage applied simultaneously to the top electrodes of the ten cantilevers while the bottom electrodes are grounded. (b) Red curve shows measured average displacement of cantilever tip $\delta_{\text{cantilever}}$ versus dc driving voltage applied simultaneously to the top electrodes of ten cantilevers. Blue curve shows the displacement of laser beam $\delta_{\text{B,laser}}$ versus dc driving voltage. The displacement of laser beam $\delta_{\text{B,laser}}$ is calculated using (1)–(3) and the values of $\delta_{\text{cantilever}}$ obtained from the red curve.

in Fig. 8, the measured attenuation curve versus dc driving voltage applied simultaneously to ten cantilevers for bending mode is shown in Fig. 9(a). As discussed earlier, bending mode is elicited when all the top electrodes of the cantilevers are biased simultaneously at the same driving voltage while all the bottom electrodes are grounded. From Fig. 9(a), a dynamic attenuation range of 40 dB was achieved when 1 V dc driving voltage was applied to the ten cantilevers. A 40 dB dynamic range is sufficient with regard to most of the commercial applications. As such, it means that the PZT MEMS VOA developed in this study will only require a dc operating voltage of 1 V.

The 40 dB attenuation achieved by 1 V dc bias in this study performed similarly to our previous data in [58], where a gimbaled PZT mirror was deployed. In addition to the piezoelectric actuated VOA mentioned above, S. H. Hung *et al.* have demonstrated a VOA consisting of an electromagnetically driven vertical mirror, achieving 35 dB attenuation at 0.4 V dc bias [6]. Fig. 9(b) was also obtained by biasing the top electrodes for all the ten cantilevers at the same voltage while the bottom electrodes were grounded. The displacement of the cantilever tips (indicated in Fig. 1), $\delta_{\text{cantilever}}$, were observed under the optical microscope, averaged, and repeated for various dc driving voltage. The data obtained were plotted and shown in the red curve of Fig. 9(b). An average cantilever tip displacement of $32 \mu\text{m}$ was obtained when the ten cantilevers are dc biased at 1 V. This displacement, in accordance to (1), is equivalent to a mechanical rotation angle $\delta_{\text{B,mirror}}$ of 1.2° . Thermal bimorph actuator has been known as a solution for large displacement under low driving voltage. This is exemplified by A. Jain, who achieved 1° mechanical deflection angle of a mirror when 1 V dc was applied to the thermal beam actuator [26]. On the other hand, a piezoelectric cantilever actuator has already demonstrated to be a prevailing solution in ac operation, e.g., oscillators and self-excited cantilever sensors for atomic force microscopes in cyclic contact mode [66]. According to our experimental data, it shows that a piezoelectric cantilever actuator can perform as well as a thermal bimorph actuator in applications based on dc operation.

The blue curve in Fig. 9(b) shows the displacement of laser beam $\delta_{\text{B,laser}}$ from its original position corresponding to minimum initial insertion loss. Values for the laser beam displacements are derived from the values obtained for cantilever tip displacements at various dc biases and substituting them into (1)–(3). From the blue curve in Fig. 9(b), it is observed that the displacement of the laser beam, $\delta_{\text{B,laser}}$, was approximately $35 \mu\text{m}$ at a dc driving voltage of 1 V, i.e., a $35 \mu\text{m}$ laser beam displacement will result in an attenuation of 40 dB for the light beam.

B. Torsional Mode

Fig. 10(a) and (b) shows the two possible biasing configurations to induce torsional mode. A potential divider was implemented to split the dc power supply into four equal potential at the potential nodes between each resistors. The potential divider is realized using four equal resistors with a resistance 20Ω , each connected in series. In Fig. 10(a), for cantilevers 1–5, the top electrodes for these cantilevers are connected to different potential nodes, while the bottom electrodes are grounded. The reverse setup is made for cantilevers 6–10, i.e., the top electrodes are grounded, while the bottom electrodes are connected to various potential nodes. In Fig. 10(b), for cantilevers 1–5, the top electrodes for these cantilevers are grounded, while the bottom electrodes are connected to different potential nodes. For cantilevers 6–10, the top electrodes are connected to the various potential nodes while the bottom electrodes are grounded. As such, each of the cantilevers in both bias cases A and B will have a different dc bias value as evidence from the look-up table in Fig. 10(c). This results in largest and zero cantilever displacement introduced at the mirror edges and center, respectively. More importantly, the generated displacements for the two sets of cantilevers are toward the opposite direction, resulting in the torsional rotation of the mirror.

Fig. 11 shows the experimental data obtained for torsional mode. Fig. 11(a) shows the measured attenuation curve versus

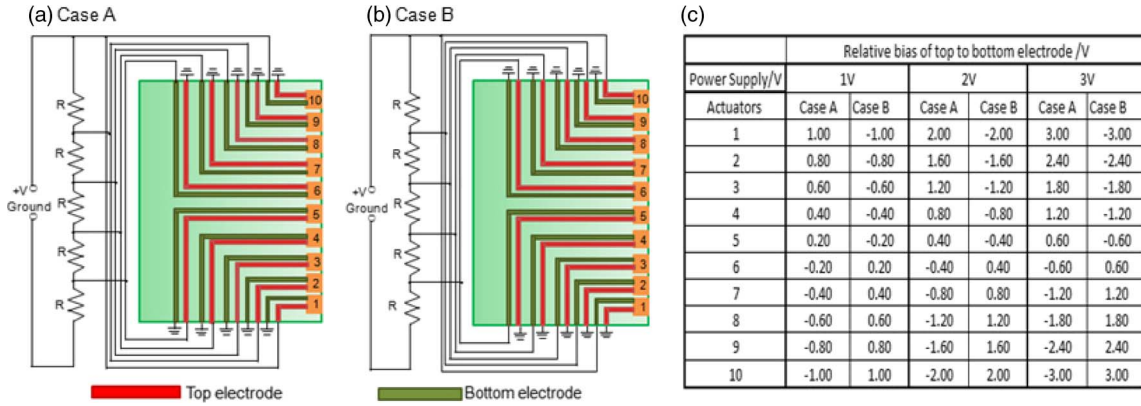


Fig. 10. Schematic drawing illustrating the electrical connections of the top and bottom electrodes of each cantilever to the dc power supply in (a) bias case A and (b) bias case B. (c) A look-up table showing the individual dc bias driving each cantilever under bias case A and B for a given dc power supply voltage.

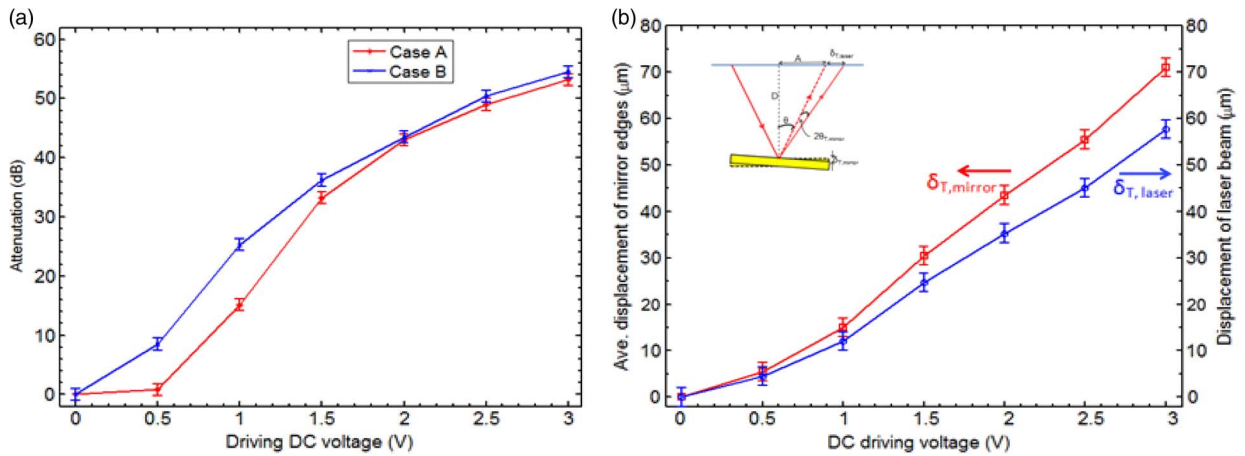


Fig. 11. Experimental data for torsional mode. (a) Measured attenuation curves versus the dc driving voltage of the power supply for both bias cases A and B. (b) Red curve shows measured average displacement of mirror edges, $\delta_{T,mirror}$, versus the dc driving voltage of power supply. Blue curve shows the displacement of te laser beam, $\delta_{T,laser}$, versus the dc driving voltage of the power supply. Both curves were obtained using bias case A. The displacement of the laser beam, $\delta_{T,laser}$, is calculated using (4)–(6) and the values of $\delta_{T,mirror}$ obtained from the red curve.

the dc voltage of the power supply. Both bias cases A and B were investigated. The attenuation of 40 dB was achieved at a bias of 1.9 V and 1.7 V for cases A and B, respectively. Although the mirror and cantilevers were arranged in symmetric layout, there was still much difficulty in aligning the laser beam to be along the far edge center of the mirror. This mainly accounted for the discrepancy of these two measured curves for different bias cases. In addition, the dimensions of the ten cantilevers may not be exactly the same due to lithography inaccuracy and deviation in fabrication process. Thus, the cantilevers under the same dc driving voltage in both bias cases may not perform the same displacement, partially contributing to the discrepancy between the two curves in Fig. 11.

In Fig. 11(b), the device is biased using case A. The absolute value for the displacements of the two opposite edges of the mirror, $\delta_{T,mirror}$, were measured, averaged, repeated for the different dc driving voltages of the power supply, and plotted as the upper-left (red) curve. The bottom-right (blue) curve for laser beam displacement, $\delta_{T,Laser}$, was derived by substituting the mirror edge displacement, $\delta_{T,mirror}$, obtained under the optical microscope into (4)–(6). From the bottom-right curve in Fig. 11(b), it can be observed that at a dc driving voltage of 1.9 V for the power supply, an approximate laser beam

displacement of 33 μm from its original position was retrieved. It means that a 33 μm laser beam displacement is needed for 40 dB attenuation of light beam in torsional mode. This value retrieved for torsional mode (33 μm) is very close to that derived from bending mode (35 μm).

C. Mixed Mode

In mixed mode operation, two dc voltages are used separately to bias cantilevers 1–5 and 6–10. Both bending and torsional mode phenomena are observed when the dc biases on both sets of cantilevers are not equivalent. As shown in Fig. 12, various driving voltage combinations were applied to the two sets of cantilevers and an attenuation characteristic topography is derived. When a dc driving voltage of 1.2 V was applied to actuators 1–5, the attenuation changes from 41 dB to 47 dB as the dc voltage applied to actuators 6–10 increased from 0 V to 2 V. For the reverse case, i.e., a dc driving voltage of 1.2 V was applied to actuators 6–10, the attenuation changes from 27 dB to 50 dB as the dc voltage applied to actuators 1–5 increased from 0 V to 2 V. This difference in attenuation characteristic between the two sets of cantilevers can be attributed to lithography inaccuracy and deviation in fabrication process.

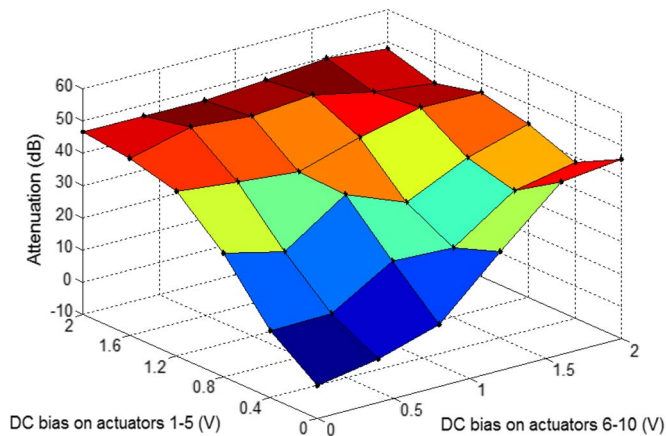


Fig. 12. Measured attenuation value as a function of dc bias applied to cantilevers 1–5 and 6–10.

As such, with mixed mode operation, an additional degree of freedom in attenuation control can be attained. More specifically, any deviation of attenuation-dc bias characteristic among various PZT MEMS VOA devices due to the fabrication process and assembly steps could be compensated by changing different driving voltages combination to the two sets of cantilevers.

VI. CONCLUSION

In this study, a novel piezoelectric-driven 3-D VOA using a mechanical supporting beam integrated with multiple cantilever actuators was explored and characterized in a 3-D attenuation configuration with a dual-core collimator. Three modes of attenuation operation have been investigated: bending, torsional, and mixed. Torsional attenuation based on the difference in the dc biasing voltage applied to piezoelectric cantilever actuators on a cantilever beam has first been demonstrated. This actuation mechanism differs greatly from those actuation mechanisms of gimbaled mirror in torsional mode, i.e., the mirror rotation is generated against the torsion spring or torsion bar. Although a thermal bimorph beam actuator has been well-characterized in terms of their capability to generate large deflection, i.e., in bending mode, no design in torsional mirror using beam actuator has been reported. Instead of using a thermal bimorph beam actuator, our unique design of piezoelectric cantilever beam actuator is the first demonstration of large torsion mirror using a beam actuator.

The bending mode operation has been concluded to be more effective in light attenuation compared to the torsional mode operation. This is exemplified by the fact that the bending mode requires a dc driving voltage of only 1 V to achieve 40 dB dynamic range during the bending mode, whereas 1.8 V is needed for the same amount of attenuation during torsional mode. The low operating voltage of 1 V allows for possible integration with other systems utilizing CMOS electronics. Further reduction of driving voltage is possible by reducing the thickness of the Si mechanical layer underneath the PZT cantilever actuators. However, the tradeoff will be the increase in deformation of the mirror surface. In addition, further reduction of the mirror size should be explored in the future as a smaller mirror size will decrease the response time of the device. The

measured transverse piezoelectric constant d_{31} for the $3.1 \mu\text{m}$ PZT layer is 136 pmV^{-1} , which implies that there is not much room for improvement of piezoelectric characteristics. A possible research direction for our device is the integration of PZT displacement sensors with the PZT attenuation mechanism. Such integration has already been successfully demonstrated by Kobayashi, where PZT driven micromirror scanner was integrated with a PZT displacement sensor [67]. Such an integration will allow the detected signals received from the displacement sensor to be used as feedback control reference. An instrument-level piezoelectric MEMS VOA with electronic feedback control circuits can hence be developed.

REFERENCES

- [1] C.-D. Liao and J.-C. Tsai, "The evolution of MEMS displays," *IEEE Trans. Ind. Electron.*, vol. 56, no. 4, pp. 1057–1065, Apr. 2009.
- [2] J. H. Lau, C. Lee, C. S. Premachandran, and Y. Aibin, *Advanced MEMS Packaging*. New York: McGraw-Hill, 2010, pp. 397–434.
- [3] A. Neukermans and R. Ramaswami, "MEMS technology for optical networking applications," *IEEE Commun. Mag.*, vol. 39, no. 1, pp. 62–69, Jan. 2001.
- [4] H. Schenk, P. Durr, D. Kunze, H. Lakner, and H. Kuck, "A resonantly excited 2D-micro-scanning-mirror with large deflection," *Sens. Actuators A, Phys.*, vol. 89, no. 1/2, pp. 104–111, Mar. 2001.
- [5] S. Sakarya, G. Vdovin, and P. M. Sarro, "Technology of reflective membranes for spatial light modulators," *Sens. Actuators A, Phys.*, vol. 97/98, pp. 468–472, Apr. 2002.
- [6] S. H. Hung, H.-T. Hsieh, and G.-D. J. Su, "An electro-magnetic micro-machined actuator monolithically integrated with a vertical shutter for variable optical attenuation," *J. Micromech. Microeng.*, vol. 18, no. 7, pp. 75 003–75 010, Aug. 2008.
- [7] S. C. Truxal, K. Kurabayashi, and Y.-C. Tung, "Design of a MEMS tunable polymer grating for single detector spectroscopy," *Int. J. Optomechanics*, vol. 2, no. 2, pp. 75–87, Apr. 2008.
- [8] Y. Du, G. Zhou, K. L. Cheo, Q. Zhang, H. Feng, and F. S. Chau, "A 2-DOF circular-resonator-driven in-plane vibratory grating laser scanner," *J. Microelectromech. Syst.*, vol. 18, no. 4, pp. 892–904, Aug. 2009.
- [9] E. Ollier, "Optical MEMS devices based on moving waveguides," *IEEE J. Sel. Topics Quantum Electron.*, vol. 8, no. 1, pp. 155–162, Jan./Feb. 2002.
- [10] R. R. A. Syms, H. Zou, J. Stagg, and H. Veladi, "Sliding-blade MEMS iris and variable optical attenuator," *J. Micromech. Microeng.*, vol. 14, no. 12, pp. 1700–1710, Dec. 2004.
- [11] M. C. Wu, L. Y. Lin, S. S. Lee, and C. R. King, "Free-space integrated optics realized by surface-micromachining," *Int. J. High Speed Electron. Syst.*, vol. 8, no. 2, pp. 283–297, 1997.
- [12] R. S. Muller and K. Y. Lau, "Surface-micromachined microoptical elements and systems," *Proc. IEEE*, vol. 86, no. 8, pp. 1705–1720, Aug. 1998.
- [13] M. C. Wu, O. Solgaard, and J. E. Ford, "Optical MEMS for lightwave communication," *J. Lightw. Technol.*, vol. 24, no. 12, pp. 4433–4454, Dec. 2006.
- [14] G. D. J. Su, H. Toshiyoshi, and M. C. Wu, "Surface-micromachined 2-D optical scanners with high-performance single-crystalline silicon micromirrors," *IEEE Photon. Technol. Lett.*, vol. 13, no. 6, pp. 606–608, Jun. 2001.
- [15] H. Toshiyoshi and H. Fujita, "Electrostatic micro torsion mirrors for an optical switch matrix," *J. Microelectromech. Syst.*, vol. 5, no. 4, pp. 231–237, Dec. 1996.
- [16] L. Y. Lin, E. L. Goldstein, and R. W. Tkach, "Free-space micromachined optical switches with submillisecond switching time for large-scale optical crossconnects," *IEEE Photon. Technol. Lett.*, vol. 10, no. 4, pp. 525–527, Apr. 1998.
- [17] J. H. Lee, Y. C. Ko, D. H. Kong, J. M. Kim, K. B. Lee, and D. Y. Jeon, "Design and fabrication of scanning mirror for laser display," *Sens. Actuators A, Phys.*, vol. 96, no. 2/3, pp. 223–230, Feb. 2002.
- [18] H. Xie, Y. Pan, and G. K. Fedder, "A CMOS-MEMS mirror with curled-hinge comb drives," *J. Microelectromech. Syst.*, vol. 12, no. 4, pp. 450–457, Aug. 2003.
- [19] D. Hah, H. S.-Y. Huang, J.-C. Tsai, J.-C. Toshiyoshi, and M. C. Wu, "Low-voltage, large-scan angle MEMS analog micromirror arrays with hidden vertical comb-drive actuators," *J. Microelectromech. Syst.*, vol. 13, no. 2, pp. 279–289, Apr. 2004.

- [20] C. Lee, "Design and fabrication of epitaxial silicon micromirror devices," *Sens. Actuators A, Phys.*, vol. 115, no. 2/3, pp. 581–591, Sep. 2004.
- [21] H. Miyajima, N. Asaoka, M. Arima, Y. Minamoto, K. Murakami, K. Tokuda, and K. Matsumoto, "A durable, shock-resistant electromagnetic optical scanner with polyimide-based hinges," *J. Microelectromech. Syst.*, vol. 10, no. 3, pp. 418–424, Sep. 2001.
- [22] A. D. Yalcinkaya, H. Urey, T. Montague, D. Brown, and R. Sprague, "Two axis electromagnetic microscanner for high resolution displays," *J. Microelectromech. Syst.*, vol. 15, no. 4, pp. 786–794, Aug. 2006.
- [23] C. H. Ji, M. Choi, S. C. Kim, K. C. Song, J. U. Bu, and H. J. Nam, "Electromagnetic two-dimensional scanner using radial magnetic field," *J. Microelectromech. Syst.*, vol. 16, no. 4, pp. 989–996, Aug. 2007.
- [24] I.-J. Cho and E. Yoon, "A low-voltage three-axis electromagnetically actuated micromirror for fine alignment among optical devices," *J. Micromech. Microeng.*, vol. 19, no. 8, p. 085 007, Aug. 2009.
- [25] S. Schweizer, S. Calmes, M. Laudon, and P. Renaud, "Thermally actuated optical microscanner with large angle and low consumption," *Sens. Actuators A, Phys.*, vol. 76, no. 1–3, pp. 470–477, Aug. 1999.
- [26] A. Jain, H. Qu, S. Todd, and H. Xie, "A thermal bimorph micromirror with large bi-directional and vertical actuation," *Sens. Actuators A, Phys.*, vol. 122, no. 1, pp. 9–15, Jul. 2005.
- [27] L. Wu and H. Xie, "Electrothermal micromirror with dual-reflective surfaces for circumferential scanning endoscopic imaging," *J. Micro/Nanolith. MEMS MOEMS*, vol. 8, no. 1, p. 013 030, Jan.–Mar. 2009.
- [28] R. Maeda, J. J. Tsaur, S. H. Lee, and M. Ichiki, "Piezoelectric microactuator devices," *J. Electroceramics*, vol. 12, no. 1/2, pp. 89–100, Jan. 2004.
- [29] Y. Yasuda, M. Akamatsu, M. Tani, T. Iijima, and H. Toshiyoshi, "Piezoelectric 2D-optical micro scanners with PZT thick films," *Integr. Ferroelectr.*, vol. 76, no. 1, pp. 81–91, Nov. 2005.
- [30] S.-J. Kim, Y.-H. Cho, H.-J. Nam, and J. U. Bu, "Piezoelectrically pushed rotational micromirrors using detached PZT actuators for wide-angle optical switch applications," *J. Micromech. Microeng.*, vol. 18, no. 12, pp. 125 022-1–125 022-7, Dec. 2008.
- [31] M. Yano, F. Yamagishi, and T. Tsuda, "Optical MEMS for photonic switching-compact and stable optical crossconnect switches for simple, fast, and flexible wavelength applications in recent photonic networks," *IEEE J. Sel. Topics Quantum Electron.*, vol. 11, no. 2, pp. 383–394, Mar./Apr. 2005.
- [32] P. De Dobbelaere, K. Falta, and S. Gloeckner, "Advances in integrated 2D MEMS-based solutions for optical network applications," *IEEE Commun. Mag.*, vol. 41, no. 5, pp. S16–S23, May 2003.
- [33] P. F. Van Kessel, L. J. Hornbeck, R. E. Meier, and M. R. Douglass, "A MEMS-based projection display," *Proc. IEEE*, vol. 86, no. 8, pp. 1687–1704, Aug. 1998.
- [34] T. S. Perry, "A dark-horse technology—The grating light valve—May join the competition to dethrone the CRT," *IEEE Spectr.*, vol. 41, no. 4, pp. 38–41, Apr. 2004.
- [35] A. Q. Liu and X. M. Zhang, "A review of MEMS external-cavity tunable lasers," *J. Micromech. Microeng.*, vol. 17, no. 1, pp. R1–R13, Jan. 2007.
- [36] C. J. Chang-Hasnain, "Tunable VCSEL," *IEEE J. Sel. Topics Quantum Electron.*, vol. 6, no. 6, pp. 978–987, Nov./Dec. 2000.
- [37] L. Y. Lin and E. L. Goldstein, "Opportunities and challenges for MEMS in lightwave communications," *IEEE J. Sel. Topics Quantum Electron.*, vol. 8, no. 1, pp. 163–172, Jan./Feb. 2002.
- [38] C. Antoine, X. Li, J.-S. Wang, and O. Solgaard, "Reconfigurable optical wavelength multiplexer using a MEMS tunable blazed grating," *J. Lightw. Technol.*, vol. 25, no. 10, pp. 3100–3107, Oct. 2007.
- [39] J. Tsai, S. T.-Y. Huang, D. Hah, and M. C. Wu, " $1 \times N^2$ wavelength selective switch with two cross-scanning one-axis analog micromirror arrays in a 4-f optical system," *J. Lightw. Technol.*, vol. 24, no. 2, pp. 897–903, Feb. 2006.
- [40] C. Lee and J. A. Yeh, "Development and evolution of MOEMS technology in variable optical attenuators," *J. Micro/Nanolith. MEMS MOEMS*, vol. 7, no. 2, p. 021 003, Apr.–Jun. 2008.
- [41] B. Barber, C. R. Giles, V. Askyuk, R. Ruel, L. Stulz, and D. Bishop, "A fiber connectorized MEMS variable optical attenuator," *IEEE Photon. Technol. Lett.*, vol. 10, no. 9, pp. 1262–1264, Sep. 1998.
- [42] C. Marxer, P. Griss, and N. F. de Rooij, "A variable optical attenuator based on silicon micromechanics," *IEEE Photon. Technol. Lett.*, vol. 11, no. 2, pp. 233–235, Feb. 1999.
- [43] X. M. Zhang, A. Q. Liu, C. Lu, and D. Y. Tang, "MEMS variable optical attenuator using low driving voltage for DWDM systems," *Electron. Lett.*, vol. 38, no. 8, pp. 382–383, Apr. 2002.
- [44] C. Lee, Y.-S. Lin, Y.-J. Lai, M. H. Tsai, C. Chen, and C. Y. Wu, "3-V driven pop-up micromirror for reflecting light toward out-of-plane direction for VOA applications," *IEEE Photon. Technol. Lett.*, vol. 16, no. 4, pp. 1044–1046, Apr. 2004.
- [45] C. Chen, C. Lee, and Y.-J. Lai, "Novel VOA using in-plane reflective micromirror and off-axis light attenuation," *IEEE Commun. Mag.*, vol. 41, no. 8, pp. S16–S20, Aug. 2003.
- [46] Y. Y. Kim, S. S. Yun, C. S. Park, J.-H. Lee, Y. G. Lee, H. K. Lee, S. K. Yoon, and J. S. Kang, "Refractive variable optical attenuator fabricated by silicon deep reactive ion etching," *IEEE Photon. Technol. Lett.*, vol. 16, no. 2, pp. 485–487, Feb. 2004.
- [47] A. Bashir, P. Katila, N. Ogier, B. Saadany, and D. A. Khalil, "A MEMS-based VOA with very low PDL," *IEEE Photon. Technol. Lett.*, vol. 16, no. 4, pp. 1047–1049, Apr. 2004.
- [48] C. Chen, C. Lee, and J. A. Yeh, "Retro-reflection type MOEMS VOA," *IEEE Photon. Technol. Lett.*, vol. 16, no. 10, pp. 2290–2292, Oct. 2004.
- [49] H. Cai, X. M. Zhang, C. Lu, A. Q. Liu, and E. H. Khoo, "Linear MEMS variable optical attenuator using reflective elliptical mirror," *IEEE Photon. Technol. Lett.*, vol. 17, no. 2, pp. 402–404, Feb. 2005.
- [50] C. Lee, "Monolithic-integrated 8CH MEMS variable optical attenuators," *Sens. Actuators A, Phys.*, vol. 123/124, pp. 596–601, Sep. 2005.
- [51] C.-H. Kim and Y.-K. Kim, "MEMS variable optical attenuator using translation motion of 45° tilted vertical mirror," *J. Micromech. Microeng.*, vol. 15, no. 8, pp. 1466–1475, Aug. 2005.
- [52] J. A. Yeh, S.-S. Jiang, and C. Lee, "MOEMS VOA using rotary comb drive actuators," *IEEE Photon. Technol. Lett.*, vol. 18, no. 10, pp. 1170–1172, May 2006.
- [53] C. Lee, "MOEMS variable optical attenuator with robust design for improved dynamic characteristics," *IEEE Photon. Technol. Lett.*, vol. 18, no. 6, pp. 773–775, Mar. 2006.
- [54] C. Lee, "A MEMS VOA using electrothermal actuators," *J. Lightw. Technol.*, vol. 25, no. 2, pp. 490–498, Feb. 2007.
- [55] K. Isamoto, K. Kato, A. Morosawa, C. Chong, H. Fujita, and H. Toshiyoshi, "A 5-V operated MEMS variable optical attenuator by SOI bulk micromachining," *IEEE J. Sel. Topics Quantum Electron.*, vol. 10, no. 3, pp. 570–578, May/Jun. 2004.
- [56] N. A. Riza and F. N. Ghauri, "Hybrid analog-digital MEMS fiber-optic variable attenuator," *IEEE Photon. Technol. Lett.*, vol. 17, no. 1, pp. 124–126, Jan. 2005.
- [57] W. Sun, W. Noell, M. Zickar, M. J. Mughal, F. Perez, N. A. Riza, and N. F. de Rooij, "Design, simulation, fabrication and characterization of a digital variable optical attenuator," *J. Microelectromech. Syst.*, vol. 15, no. 5, pp. 1190–1200, Oct. 2006.
- [58] C. Lee, F.-L. Hsiao, T. Kobayashi, K. H. Koh, P. V. Ramana, W. Xiang, B. Yang, C. W. Tan, and D. Pinjala, "A 1-V operated MEMS variable optical attenuator using piezoelectric PZT thin-film actuators," *IEEE J. Sel. Top. Quantum Electron.*, vol. 15, no. 5, pp. 1529–1536, Sep./Oct. 2009.
- [59] H. Yu, G. Zhou, F. S. Chau, and F. Lee, "A variable optical attenuator using optofluidic technology," *J. Micromech. Microeng.*, vol. 18, no. 11, pp. 115 016-1–115 016-5, Nov. 2008.
- [60] M. I. Lapsley, S.-C. S. Lin, X. Mao, and T. J. Huang, "An in-plane, variable optical attenuator using a fluid-based tunable reflective interface," *Appl. Phys. Lett.*, vol. 95, no. 8, pp. 083 507-1–083 507-3, Aug. 2009.
- [61] J. G. Smits and W.-S. Choi, "The constituent equations of piezoelectric heterogeneous bimorphs," *IEEE Trans. Ultrason., Ferroelectr., Freq. Control*, vol. 38, no. 3, pp. 256–270, May 1991.
- [62] T. Kobayashi, M. Ichiki, T. Noguchi, K. Nakamura, and R. Maeda, "Deflections of wagers and cantilevers with Pt/LNO/PZT/LNO/Pt/Ti/SiO₂ multilayered structures," *Thin Solid Films*, vol. 516, no. 16, pp. 5272–5276, Jun. 2008.
- [63] T. Kobayashi, M. Ichiki, R. Kondou, K. Nakamura, and R. Maeda, "Fabrication of piezoelectric microcantilevers using LaNiO₃ buffered Pb(Zr, Ti)O₃ thin film," *J. Micromech. Microeng.*, vol. 18, no. 3, pp. 035 0007-1–035 007-5, Mar. 2008.
- [64] T. Kobayashi, M. Ichiki, J. Tsaur, and R. Maeda, "Effect of multi-coating process on the orientation and microstructure of lead zirconate titanate (PZT) thin films derived by chemical solution deposition," *Thin Solid Films*, vol. 489, no. 1/2, pp. 74–78, Oct. 2005.
- [65] N. Sama, C. Soyer, D. Remiens, C. Verrue, and R. Bouregba, "Bottom and top electrodes nature and PZT film thickness influence on electrical properties," *Sens. Actuators A, Phys.*, vol. 158, no. 1, pp. 99–105, Mar. 2010.
- [66] C. Lee, T. Itoh, and T. Suga, "Self-excited piezoelectric PZT microcantilevers for dynamic SFM—With inherent sensing and actuating capabilities," *Sens. Actuators A, Phys.*, vol. 72, no. 2, pp. 179–188, Jan. 1999.
- [67] T. Kobayashi, R. Maeda, T. Itoh, and R. Sawada, "Smart optical microscanner with piezoelectric resonator, sensor and tuner using Pb(Zr, Ti)O₃ thin film," *Appl. Phys. Lett.*, vol. 90, no. 18, pp. 183 514-1–183 514-3, Apr. 2007.



Kah How Koh received the B.Eng. degree from the Department of Electrical and Computer Engineering, National University of Singapore (NUS), Singapore, in 2009. He is currently working toward the Ph.D degree at NUS under the sponsorship of GLOBAL-FOUNDRIES, Singapore.

His research interests include optical micro-electromechanical systems, focusing mainly on scanning mirrors and variable optical attenuators.



Chengkuo Lee (S'93–M'96) received the M.S. degree in materials science and engineering from National Tsing Hua University, Hsinchu, Taiwan, in 1991, the M.S. degree in industrial and system engineering from Rutgers University, New Brunswick, NJ, in 1993, and the Ph.D. degree in precision engineering from The University of Tokyo, Tokyo, Japan, in 1996.

He worked as a Foreign Researcher in the Nanometerscale Manufacturing Science Laboratory of the Research Center for Advanced Science and Technology, The University of Tokyo, from 1993 to 1996. He had also worked in the Mechanical Engineering Laboratory, AIST, MITI of Japan as a JST Research Fellow in 1996. Thereafter, he became a Senior Research Staff Member of the Microsystems Laboratory, Industrial Technology Research Institute, Hsinchu, Taiwan. In September 1997, he joined Metrodyne Microsystem Corporation, Hsinchu, Taiwan, and established the MEMS device division and the first micromachining fab for commercial purposes in Taiwan. He was the Manager of the MEMS device division between 1997 and 2000. He was an Adjunct Assistant Professor in the Electro-physics Department of National Chiao Tung University, Hsinchu, Taiwan, in 1998, and an Adjunct Assistant Professor in the Institute of Precision Engineering of National Chung Hsing University, Taichung, Taiwan, from 2001 to 2005. In August 2001, he cofounded Taiwan's Asia Pacific Microsystems, Inc., where he first became Vice President of R&D, before becoming Vice President of the optical communication business unit and Special Assistant to the Chief Executive Officer in charge of international business and technical marketing for the MEMS foundry service. From 2006 to 2009, he was a Senior Member of the Technical Staff at the Institute of Microelectronics, A*Star, Singapore. He has been an Assistant Professor in the Department of Electrical and Computer Engineering, National University of Singapore, Singapore, since December 2005. He is the coauthor of *Advanced MEMS Packaging* (McGraw-Hill, 2010). He has contributed to more than 130 international conference papers and extended abstracts and 80 peer-reviewed international journal articles in the fields of MEMS, nanophotonics, and nanotechnology. He is also the holder of nine U.S. patents.



Takeshi Kobayashi received the B.S., M.S. and Ph.D. degrees in materials science from The University of Tokyo, Tokyo, Japan.

He was a Researcher at the National Institute of Advance Industrial Science and Technology, Tsukuba, Japan. His research interests include piezoelectric MEMS devices and their application to wireless sensor networks. He has contributed to more than 50 international journal papers and conference proceedings papers. Two of his recent publications have been selected as highlighted papers of the

Journal of Micromechanics and Microengineering in 2007 and 2008.